Supplementary Information for

Flatband and Indirect Bandgap Cocrystals for Efficient Photothermal Conversion

Chao Ge[1†*], Qiyuan Xie[1†], Jinke Jiang[2], Yachao Li[3], Xiaoran Ma[3], Siyu Wang[4], Danmin Liu[4], Tao Chen[1], Haiying Song[1*], Wenkai Zhang[3*], Yang Liu[2*]

1School of Physics and Optoelectronic Engineering, Beijing University of Technology, Beijing 100124, China

2State Key Laboratory of Crystal Materials, Shandong University, Jinan 250100, China

3School of Physics and Astronomy, Applied Optics Beijing Area Major Laboratory, Center for Advanced Quantum Studies, Beijing Normal University, Beijing 100875, China

4Key Laboratory of Advanced Functional Materials, College of Materials Science and Engineering, Beijing University of Technology, Beijing 100124, China

*E-mail: gechao@bjut.edu.cn; hysong@bjut.edu.cn; wkzhang@bnu.edu.cn; liuyangicm@sdu.edu.cn

[†]These authors contributed equally to this work.

Table of Contents

Figure S16. Cooling curves of the three cocrystals after 808 nm laser irradiation at 0.40 W/cm^2 and their corresponding time-ln (θ) linear curve.

Table S1. Summary of X-ray crystallographic data for TCO, 2FCO and 4FCO.

Table S2. Carrier relaxation dynamics fitting of TCO at specific wavelengths.

Table S3. Carrier relaxation dynamics fitting of 2FCO at specific wavelengths.

Table S4. Carrier relaxation dynamics fitting of 4FCO at specific wavelengths.

Table S5. Calculation data of the photothermal conversion efficiency.

Table S6. Calculation data of the solar-to-vapor conversion efficiency.

Supplementary Note 1. Calculation of the photothermal conversion efficiency.

Supplementary Note 2. Calculation of the solar-to-vapor conversion efficiency.

Supplementary References

Supplementary Movie:

Movie S1. Application of 4FCO photothermal cocrystal in water evaporation. Water vapor floating on 4FCO-PU foam can be clearly observed with the naked eye under 3 suns of irradiation.

Movie S2. 4FCO-PTE device used as a power supply to drive bulbs. (Size of PTE: 5.0 cm× 5.0 cm under 3 suns of irradiation, or size of PTE: 7.5 cm×7.5 cm under 1 sun)

Movie S3. 4FCO-PTE device used as a power supply to drive fans. (Size of PTE: 5.0 cm×5.0 cm under 3 suns of irradiation, or size of PTE: 7.5 cm×7.5 cm under 1 sun)

Movie S4. 4FCO-PTE device used as a power supply to drive mobile phones. (Size of PTE: 5.0 cm×5.0 cm under 3 suns of irradiation, or size of PTE: 7.5 cm×7.5 cm under 1 sun)

Figure S1. Photos of TCO, 2FCO, 4FCO cocrystals and their monomers.

Table S1 Summary of X-ray crystallographic data for TCO, 2FCO and 4FCO

Crystal	TCO	**2FCO**	4FCO
CCDC	251572	**2387616 (New deposition)**	1024222
Crystal system	Monoclinic	Monoclinic	Triclinic
Chemical formula	$C_{36}H_{16}N_4$	$C_{60}H_{26}F_2N_4$ $C_{12}H_2F_2N_4$, $2(C_{24}H_{12})$	$C_{36}H_{12}F_4N_4$
Space group	P1 2_1/c 1	P 1 2_1/n 1	P-1
Z	2	2	1
Formula weight	504.55	840.85	576.51
Colour	black	dark green	dark green
a(Å)	10.9241(4)	10.5994(2)	7.0039(6)
b(Å)	7.1691(5)	9.7322(2)	8.6312(8)
c(Å)	15.8491(10)	19.1707(4)	11.3183(10)
α(Å)	90	90	109.504(1)
β(Å)	106.598(2)	93.164(1)	104.794(1)
γ(Å)	90	90	90.131(1)
V(Å^3)	1189.52(12)	1974.55(7)	620.69(10)
Density (g/cm^2)	1.409	1.414	1.542
Collected reflns	8798	19089	5995
Unique reflns	1696	4013	2193
Parameters	181	525	199
Rint	0.042	0.0555	0.0104
$R_1[I>2\sigma(I)]$	0.0373	0.0652	0.0309
wR_2(All reflections)	0.0926	0.1911	0.0911
GOF	0.8710	1.080	1.066

$R_1 = \Sigma||F_o| - |F_c||/|F_o|$; $wR_2 = [\Sigma[w(F_o^2 - F_c^2)^2]/\Sigma w(F_o^2)^2]^{1/2}$; $w = 1/[\sigma^2(F_o)^2 + (aP)^2 + bP]$, where $P = [F_o^2 + 2F_c^2]/3$

The crystal structure analysis was carried out on a Bruker SMART APEX-II equipped with CCD area-detector diffractometer using graphite-monochromated Cu$_{\text{Ká}}$ radiation (λ = 1.54178 Å) with the w scan method. The structures were solved by direct methods and refined by full-matrix least-squares technique on F^2 using SHELX programs. The crystallographic data of 2FCO have been deposited in the Cambridge Crystallographic Data centre (CCDC 2387616). The crystallographic data for TCO and 4FCO are obtained directly from the CCDC.[1,2]

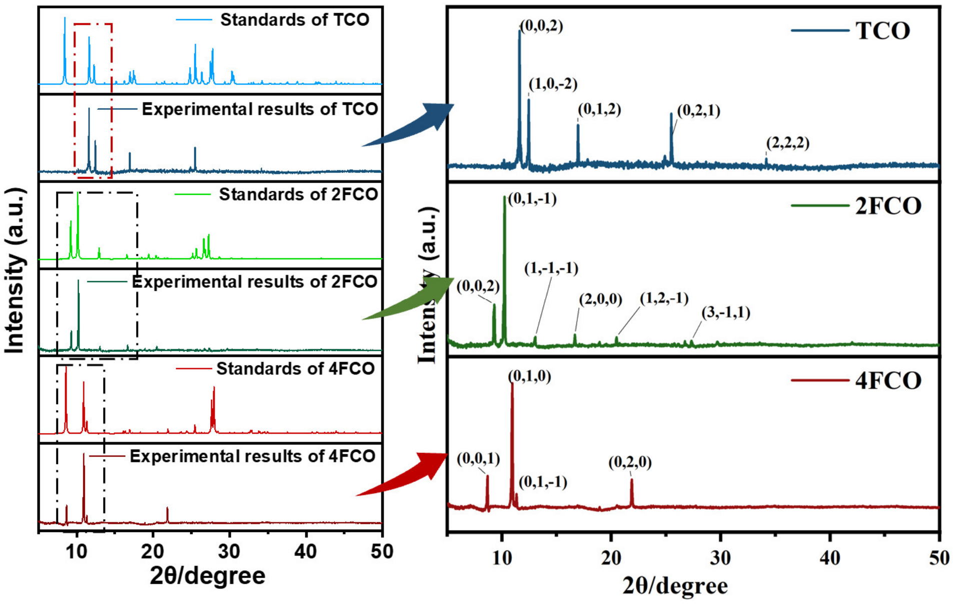

Figure S2. The powder X-ray diffraction (XRD) patterns of the three cocrystals. The diffraction peaks are in good agreement with the corresponding calculated results and are depicted by Miller indices. The sharpness of the diffraction peaks indicates that the three cocrystals exhibit good crystallinity.

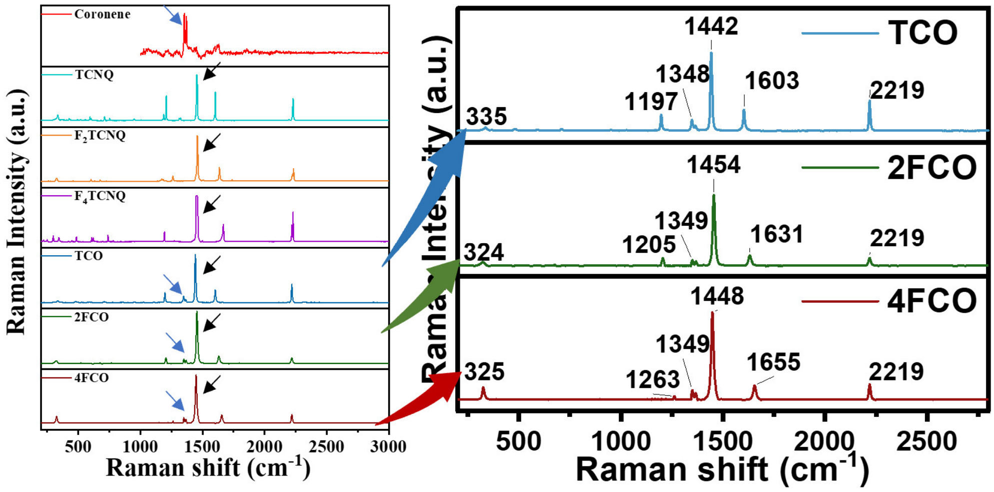

Figure S3. Raman spectra of the three cocrystals and their monomers. The vibrational modes in the cocrystals indeed reflect a combination of coronene and F_xTCNQ monomer components but with subtle changes in peak positions. For instance, the characteristic peaks at 1442 cm^{-1} for TCO, 1454 cm^{-1} for 2FCO and 1448 cm^{-1} for 4FCO exhibit a downshift compared to F_xTCNQ (around 1456 cm-1). These specific peaks correspond to the strong C=C in-plane stretching mode (Ag symmetry) within F_xTCNQ molecules, which are sensitive to the electronic densities.[3] Thus the observed shifts in cocrystals can serve as an indication for the occurrence of intermolecular charge transfer.

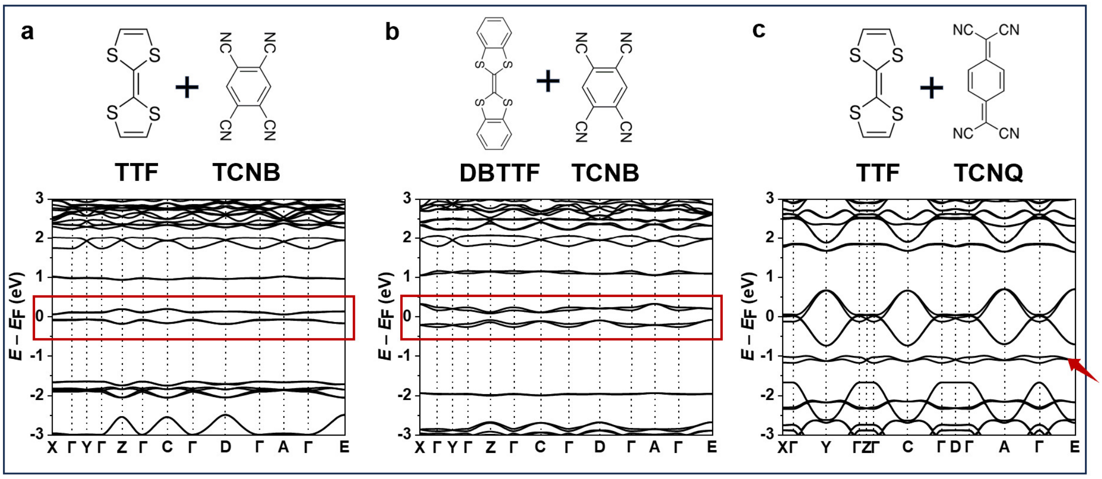

Figure S4. Flatband electronic structures near E_F in the Brillouin zone, calculated by density functional theory (DFT) for TBC cocrystal (a), DTC cocrystal (b) and TQC cocrystal (c). The absorption spectra of the cocrystals in the literature show absorption cutoff edges of 1190 nm (TBC), 903 nm (DTC), and over 2500 nm (TQC), highlighting their effective light-harvesting abilities.[4]

Notably, the metallic TQC cocrystal exhibits relatively uniform absorption across the 200−2500 nm range, attributed to both intraband and interband optical transitions. The near-infrared absorption corresponds to intraband transitions within partially filled states near E_F, while the ultraviolet-visible absorption involves interband transitions from the low-lying flatband to higher energy orbitals.[5] This low-lying flatband enhances solar spectral absorption in the ultraviolet-visible region.

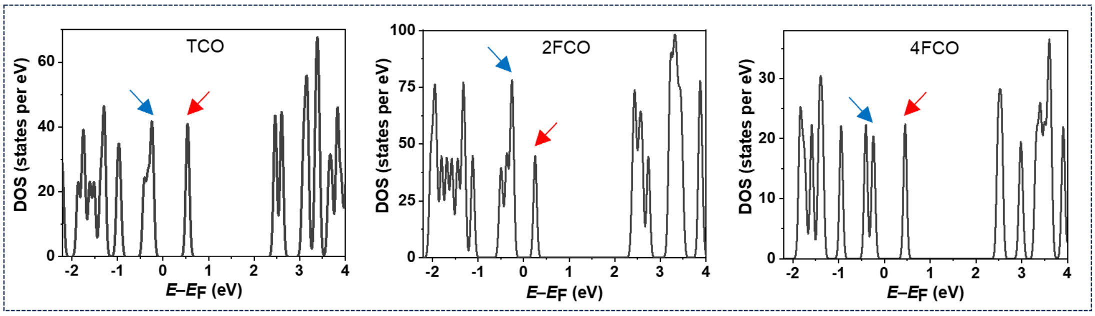

Figure S5. Calculated partial densities of states of the three cocrystals. The blue and red arrows indicate the DOS at the top of the valence band and the bottom of the conduction band, respectively. It can be seen that the flatband electronic structure (see **Figure 1c-e** in the main text) exhibits low energy dispersion and relatively high density of states (DOS), which increases the effective joint density of states (JDOS) available for interaction in the valence and conduction bands of the cocrystals, thereby improving their ability to absorb light and generate charge carriers.

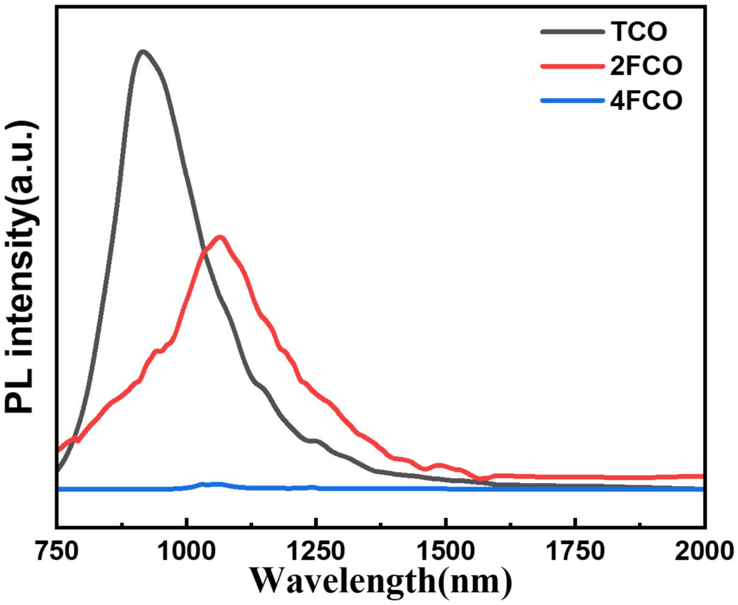

Figure S6. Steady-state photoluminescence spectra of the three cocrystals.

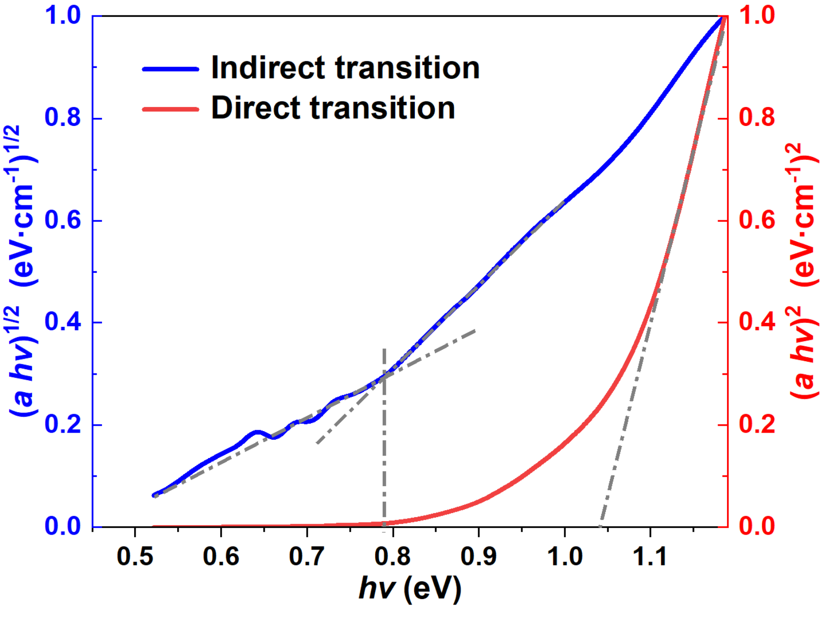

Figure S7. Tauc's plot for direct (red) and indirect (blue) band transitions of 4FCO cocrystal. The curves of $(\alpha hv)^2$ and $(\alpha hv)^{1/2}$ versus photon energy (hv), derived from the absorption spectra, fit well with the Tauc model. Tauc's relation is expressed as $(\alpha hv)^{1/n} = C \times (hv - Eg)$, where hv is the incident photon energy, C is the proportionality constant, Eg is the band gap energy, and n = 1/2 and 2 for direct and indirect band gap, respectively.

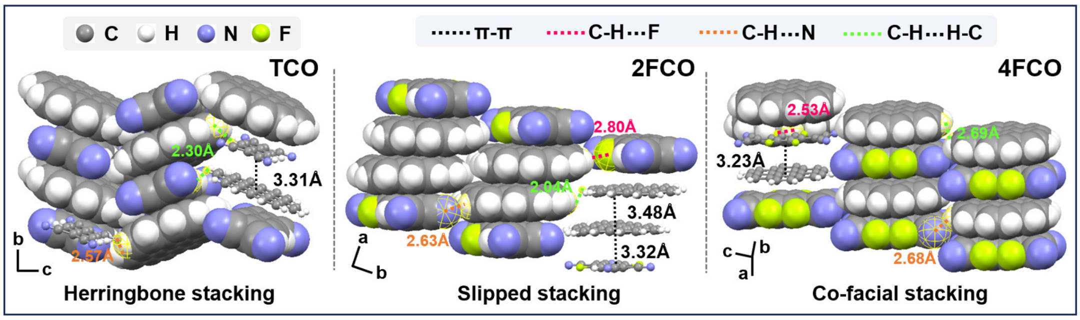

Co-crystal	D-A angle	D-A distance	C-H…N distance	C-H…F distance
TCO	45.37°	3.31-3.32 Å	2.570 Å	/
2FCO	32.27°	3.32-3.48 Å	2.630 Å	2.80 Å
4FCO	parallel	3.23-3.24 Å	2.676 Å	2.53 Å

Figure S8. The molecular packing geometry and intermolecular interaction of the three cocrystals.

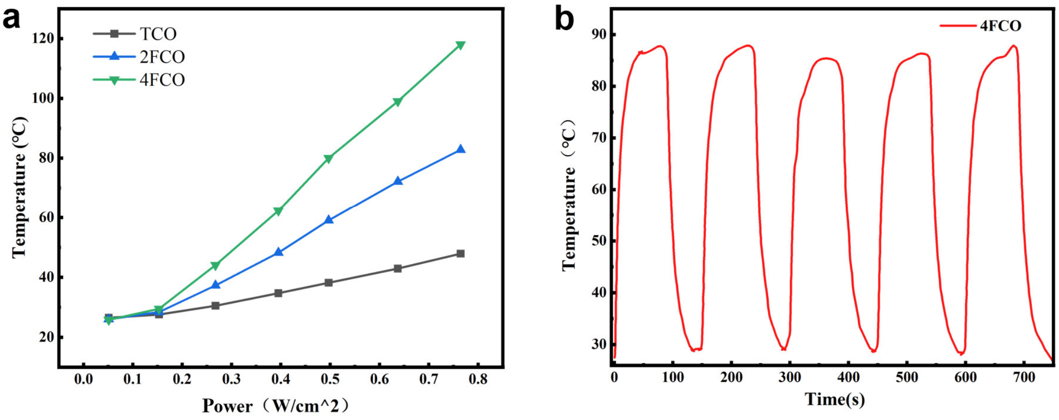

Figure S9. Laser power-dependent and multi-cycle photothermal tests. (a) Temperature changes of the three cocrystals dependent on different powers of irradiation laser. **(b)** Photothermal stability performance of 4FCO upon cyclic on-off irradiation of 0.55 W/cm^2.

Table S2. Carrier relaxation dynamics fitting of TCO at specific wavelengths. (pump laser fluence: ~184 μJ/cm^2)

Fitting Function	$\Delta A = A_1 * \exp(-t/\tau_1) + A_2 * \exp(-t/\tau_2) + A_0$			
Probe wavelength	552 nm	650 nm	**764 nm**	1100 nm
A_1	0.45818 ± 0.03402	-12.633 ±--	-0.55998 ± 0.03445	0.6492 ± 0.14558
τ_1 (ps)	0.82358 ± 0.09916	0.00533 ±--	**0.76906 ± 0.07074**	0.46937 ± 0.12243
A_2	0.25961 ± 0.01235	-0.15693 ± 442482.19484	-0.73132 ± 0.0207	0.25695 ± 0.02478
τ_2 (ps)	46.04598 ± 7.02267	70.99713 ± 5.2096E-8	**81.15223 ± 6.12455**	40.04067 ± 11.65468

Table S3. Carrier relaxation dynamics fitting of 2FCO at specific wavelengths. (pump laser fluence: ~184 μJ/cm^2)

Fitting Function	$\Delta A = A_1 * \exp(-t/\tau_1) + A_2 * \exp(-t/\tau_2) + A_0$			
Probe wavelength	632 nm	750 nm	**905 nm**	1155 nm
A_1	0.22933 ± 0.10302	-0.03195 ± 0.01501	-0.14694 ± 0.01567	2.70551 ± 4.24591
τ_1 (ps)	0.41296 ± 0.15996	8.74796 ± 7.55582	**6.11571 ± 1.12057**	0.13556 ± 0.06925
A_2	0.28389 ± 0.00949	-0.12147 ± 0.01585	-0.62291 ± 0.01207	0.07894 ± 0.01707
τ_2 (ps)	26.79679 ± 2.35448	85.28157 ± 16.17359	**65.83135 ± 4.55928**	9.99797 ± 5.19831

Table S4. Carrier relaxation dynamics fitting of 4FCO at specific wavelengths. (pump laser fluence: ~184 μJ/cm^2)

Fitting Function	$\Delta A = A_1 * \exp(-t/\tau_1) + A_2 * \exp(-t/\tau_2) + A_0$			
Probe wavelength	605 nm	813 nm	**1016 nm**	1180 nm
A_1	0.49382 ± 0.06346	-0.16046 ± 0.03058	-1.43631 ± 0.10318	0.40588 ± 0.08751
τ_1 (ps)	0.2428 ± 0.02356	0.42199 ± 0.09656	**0.36828 ± 0.02959**	0.53372 ± 0.163
A_2	0.20482 ± 0.00415	-0.37078 ± 0.00613	-0.88597 ± 0.01814	0.13111 ± 0.02512
τ_2 (ps)	8.88637 ± 0.4215	13.16879 ± 0.41973	**9.57247 ± 0.40391**	17.20988 ± 7.22252

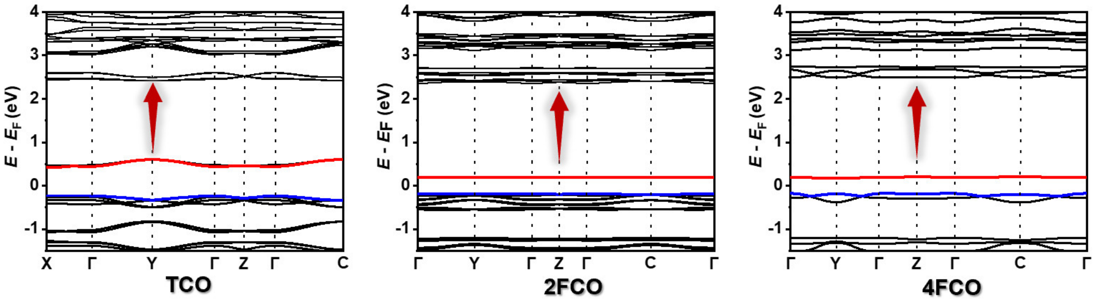

Figure S10. Calculated electronic band structures of the three cocrystals correspond to the absorption transitions of the first excited state. The results emphasized the energy gap between the first exited state and the second exited state, of which the transitions between the corresponding two levels are coincident with the PA_1 bands in transient absorption (TA) spectroscopy.

	TCO	2FCO	4FCO
LUMO	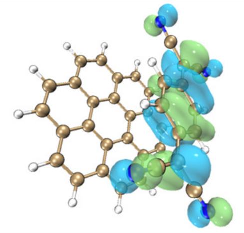	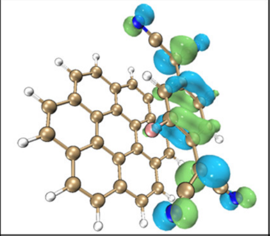	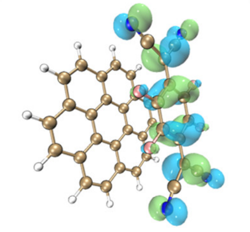
HOMO	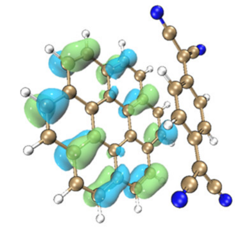	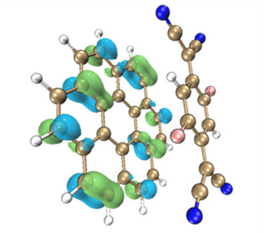	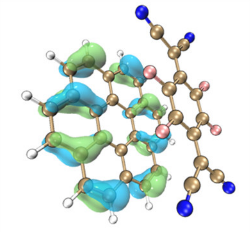

Figure S11. Calculated molecular orbital diagram of the three cocrystals. The electron cloud in the highest occupied molecular orbital (HOMO) is mainly concentrated on the electron-donor, coronene, while the electrons in the lowest unoccupied molecular orbital (LUMO) are predominantly distributed on the acceptor, F_xTCNQ, indicating significant intermolecular charge transfer and redistribution.

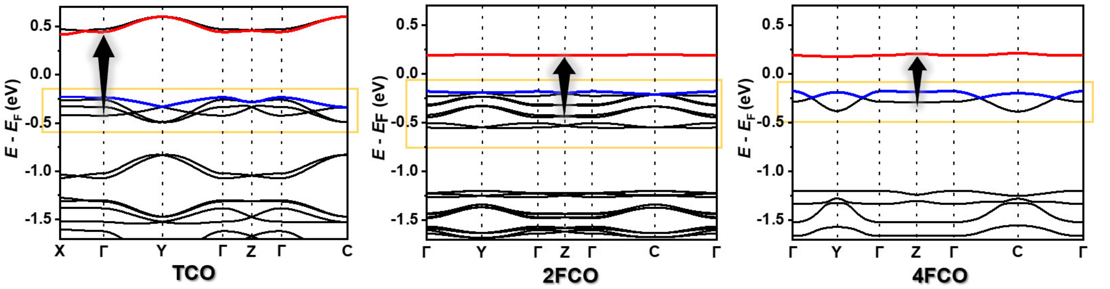

Figure S12. Calculated electronic band structures of the three cocrystals correspond to the transitions of the lower valence band. The results emphasized the transitions from a lower valence band to the conduction band minimum (the small PB_2 bands in TA spectroscopy). The lower valence band energy level, indicated in the yellow box, coincides with the photobleaching wavelength.

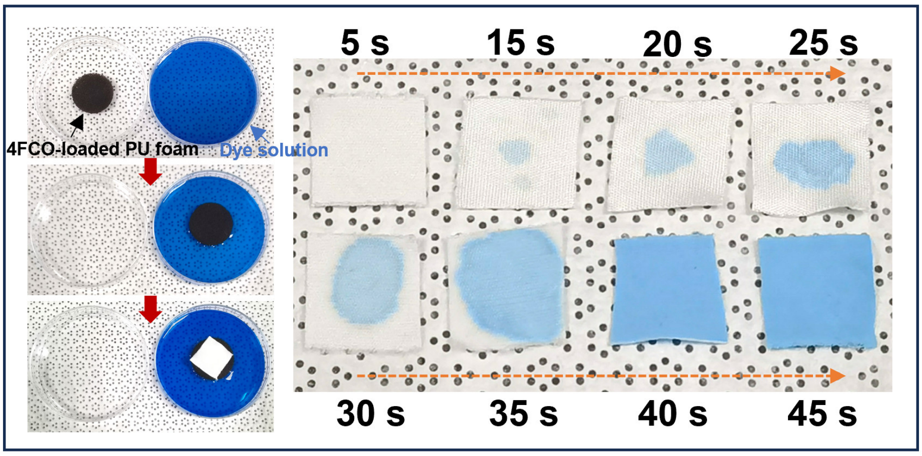

Figure S13. The capillary condensation transport experiment of 4FCO-loaded PU foam. Dyeing process display of water absorption in 45 seconds of the 4FCO-loaded PU foam.

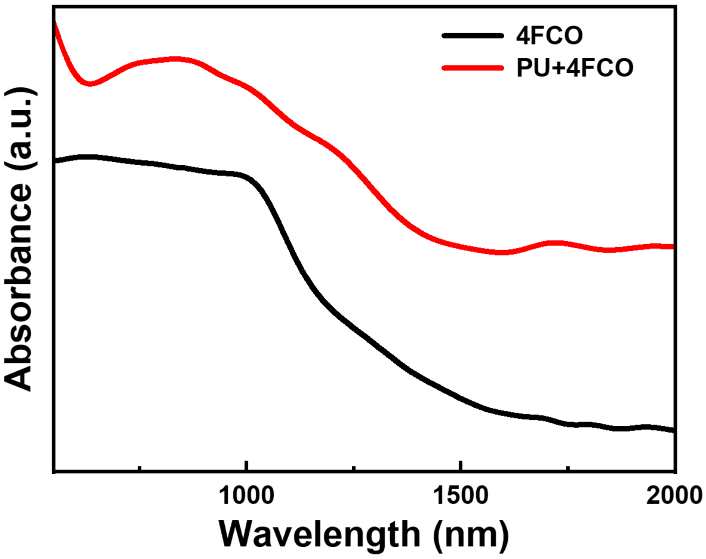

Figure S14. Steady-state absorption spectra of 4FCO and 4FCO-loaded PU foam. The results indicate that PU foam plays a positive role in trapping sunlight due to the multiple light reflections occurring within its hierarchical micro-pores.

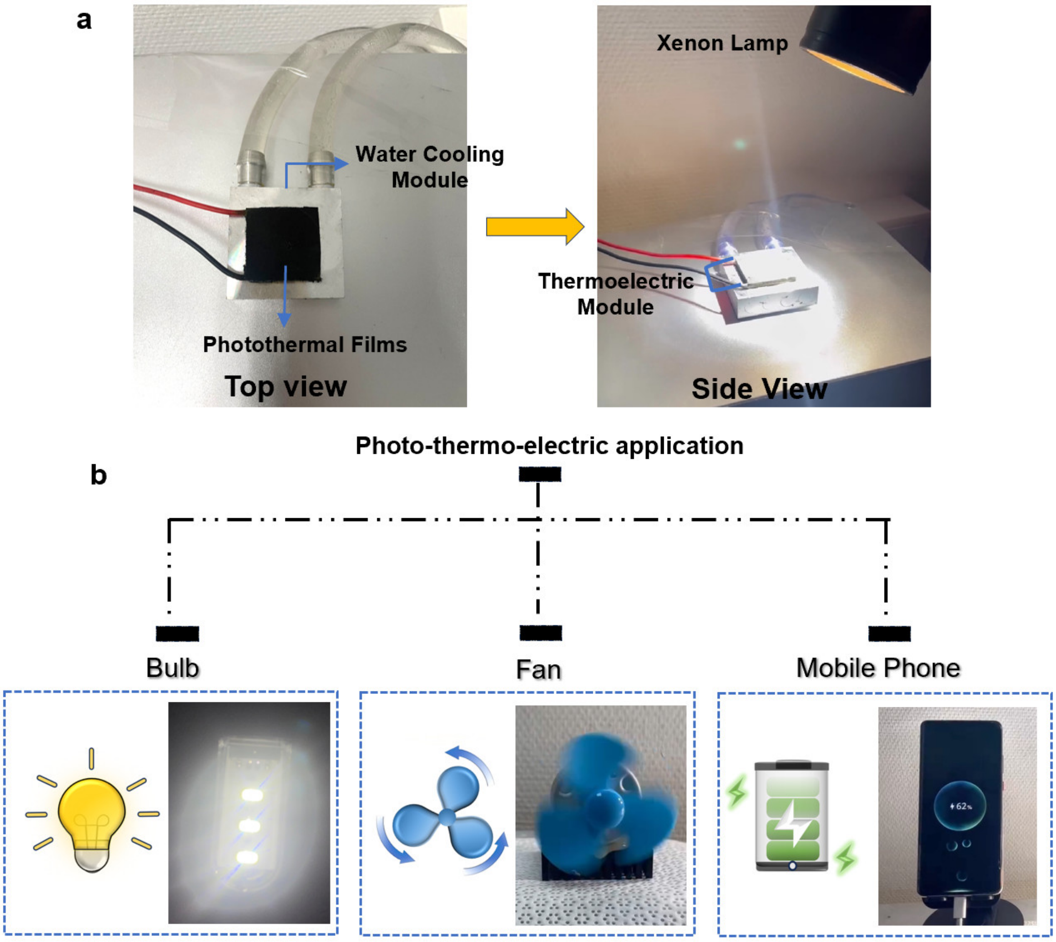

Figure S15. Photo-thermo-electric (PTE) device integration and the electrical performance application. (a) Top and side views of PTE conversion device photos. **(b)** Application photos of 4FCO-PTE device used as a power supply to drive bulbs, fans and mobile phones.

It should be noted that once the type and thickness of the photothermal material, as well as the type of thermoelectric (TE) device, are fixed, the final electrical output depends on the size of the TE device (thermoelectric pairs). For example, when powering devices such as fans, bulbs, or mobile phones with the help of a booster module, a 5.0 cm × 5.0 cm PTE device requires 3 suns of irradiation, whereas a 7.5 cm × 7.5 cm PTE device requires only 1 sun of irradiation.

Supplementary Notes

Supplementary Note 1. *Calculation of the photothermal conversion efficiency*

The infrared imager was used to record the photothermal process of three cocrystals (film thickness: 200 nm) under 808 nm laser irradiation. The photothermal conversion efficiency η is calculated as follows[6]:

Firstly, based on the total energy conservation of the system,

$$\sum_i m_i C_{p,i} \frac{dT}{dt} = Q_S - Q_{LOSS}$$

Among them, m_i and $C_{p,i}$ represent mass and specific heat capacity, respectively. The system contains cocrystal samples and thin quartz substrates, so the formula can be further expanded as follows:

$$\sum_i m_i C_{p,i} = m_{Sample} \times C_{Sample} + m_{quartz} \times C_{quartz}$$

Q_S and Q_{LOSS} represent the photothermal energy input into the system and the thermal energy lost to the surrounding environment when the near-infrared laser irradiates the cocrystal samples, respectively. When Q_S and Q_{LOSS} are equal, that is, the temperature in the system reaches the maximum, the system is in equilibrium:

$$Q_S = Q_{LOSS} = hS\Delta T_{max}$$

Where h is the heat transfer coefficient, S is the surface area of the system, and ΔT_{max} is the maximum temperature difference value. The photothermal conversion efficiency η is calculated as follows:

$$\eta = \frac{hS\Delta T_{max}}{I(1 - 10^{-A_{808}})}$$

Where I is the laser power (0.40 W/cm^2), and A_{808} is the absorbance of the cocrystals at 808 nm. In order to obtain hS, a dimensionless driving force temperature Θ and a system time constant τ_s are introduced as follows:

$$\Theta = \frac{T - T_{surr}}{T_{max} - T_{surr}}$$

$$\tau_s = \frac{\sum_i m_i C_{p,i}}{hS}$$

Where T is the temperature of the cocrystals, T_{max} is the highest temperature of the system, and T_{surr} is the initial temperature of the environment (24.1°C).

$$\frac{d\Theta}{dt} = \frac{1}{\tau_s}\frac{Q_S}{hS\Delta T_{max}} - \frac{\Theta}{\tau_s}$$

When the laser stops irradiation, $Q_S = 0$, that is, $\frac{d\Theta}{\mathrm{dt}} = -\frac{\Theta}{\tau_s}$, $t = -\tau_s ln\Theta$. We can calculate hS by calculating the slope of the cooling time versus $ln\Theta$. Thus, the time constant τ_s and the photothermal conversion efficiency η in the system are obtained.

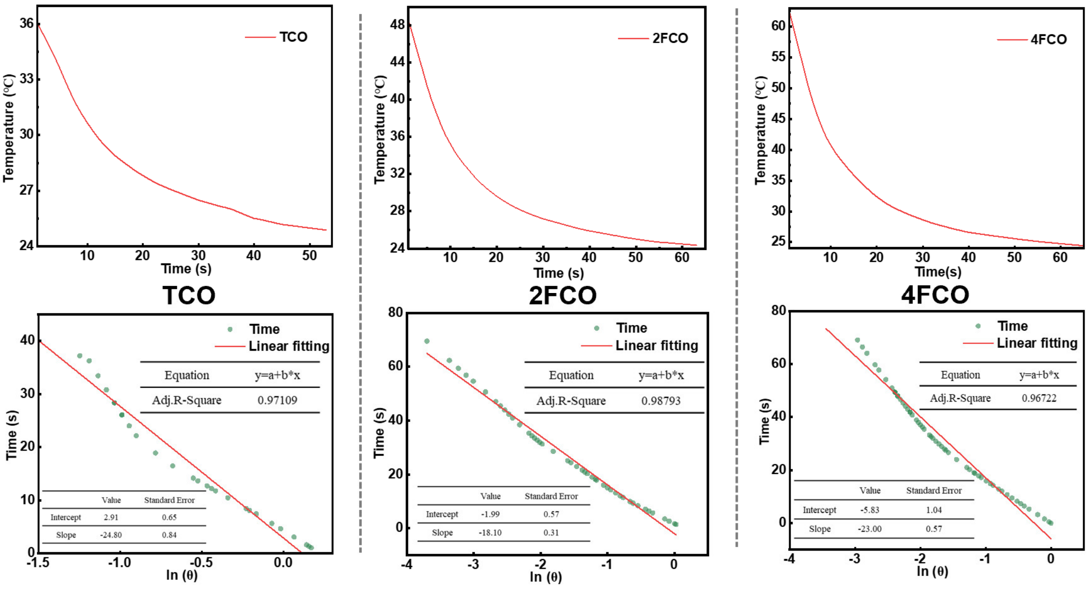

Figure S16. Cooling curves of the three cocrystals after 808 nm laser irradiation at 0.40 W/cm^2 and their corresponding time-ln (θ) linear curve.

From the corresponding temperature cooling curves under off radiation, the τ_s for TCO, 2FCO, and 4FCO were fitted to be 24.8 s, 18.1 s and 23.0 s respectively. Consequently, the photothermal conversion efficiencies were calculated to be 25.15%, 53.40%, and 72.89%, for TCO, 2FCO, and 4FCO respectively. The detailed calculation parameters are shown in **Table S5**.

Table S5. Calculation data of the photothermal conversion efficiency

value	quartz	TCO	2FCO	4FCO
m (g)	0.23	0.0005	0.0005	0.0005
$C_{\mathrm{p,i}}$ (J (g °C)$^{-1}$)	0.76	0.70	0.60	0.65
$m_{\mathrm{i}}C_{\mathrm{p,i}}$	0.1748	0.00035	0.0003	0.000325
ΔT_{max} (°C)	/	11.6	24.1	38.2
A^{808}	/	0.570	0.903	0.954
τ_s (s)	/	24.8	18.1	23.0

Supplementary Note 2. *Calculation of the solar-to-vapor conversion efficiency*

The solar-to-vapor conversion efficiency η is calculated as follows[7]:

$$\eta = \frac{mh_{LV}}{C_{opt}P_0}$$

$$m = m_{light} - m_{dark}$$

$$h_{LV} = Q + \Delta h_{vap}$$

Where m refers to the solar water evaporation rate, h_{LV} refers to the sensible heat and the enthalpy of the total liquid-vapor phase-change, C_{opt} is the optical concentration of 1, and P_0 is the nominal irradiation value of 1 kW m^{-2}. m_{light} refers to the water evaporation rate under solar illumination, while m_{dark} refers to the water evaporation rate under dark conditions. Q is the energy to heat the system from the initial temperature T_0 to the final temperature T, and Δh_{vap} is the latent heat of vaporization of water.

$$Q = C_{liquid} \times (T - T_0)$$

$$\Delta h_{vap} = Q_1 + \Delta h_{100} + Q_2$$

$$Q_1 = C_{liquid} \times (100 - T)$$

$$Q_2 = C_{vapor} \times (T - 100)$$

C_{liquid} and C_{vapor} are the specific heat capacities of liquid water and water vapor respectively. Δh_{100} is the is the latent heat of vaporization of water at 100 °C. Q_1 refers to the energy for liquid water to heat from temperature T to 100 °C. Q_2 refers to the energy for water vapor to drop from 100 °C to T.

Based on the experimental results, when the optimal loading mass is 11.52 mg, the 4FCO-loaded PU foam achieved a maximum water evaporation rate of 1.51 kg m^{-2} h^{-1} under 1 solar irradiance, and the solar-to-vapor conversion efficiency (η) were calculated to be 96.64 %. The detailed calculation parameters are shown in **Table S6**.

Table S6. Calculation data of the solar-to-vapor conversion efficiency

Parameter	Value	Parameter	Value
C_{liquid} (J (g °C)$^{-1}$)	4.18	Δh_{100} (kJ/kg)	2260
C_{vapor} (J (g °C)$^{-1}$)	1.865	Δh_{vap} (kJ/kg)	2405.382
T_0 (°C)	22.1	h_{LV} (kJ/kg)	2468.5
T (°C)	37.2	m_{dark} (kg m^{-2} h^{-1})	0.1000
Q (kJ/kg)	63.118	m_{light} (kg m^{-2} h^{-1})	1.5094

References

1 Chi X, Besnard C, Thorsmølle V K, et al. Structure and transport properties of the charge-transfer salt coronene− TCNQ[J]. Chemistry of materials, 2004, 16(26): 5751-5755.

2 Yoshida Y, Kumagai Y, Mizuno M, et al. Improved dynamic properties of charge-transfer-type supramolecular rotor composed of coronene and F4TCNQ[J]. Crystal Growth & Design, 2015, 15(11): 5513-5518.

3 Hu P, Du K, Wei F, et al. Crystal growth, HOMO–LUMO engineering, and charge transfer degree in perylene-F x TCNQ (x= 1, 2, 4) organic charge transfer binary compounds[J]. Crystal Growth & Design, 2016, 16(5): 3019-3027.

4 Tian S, Huang Z, Tan J, et al. Manipulating interfacial charge-transfer absorption of cocrystal absorber for efficient solar seawater desalination and water purification[J]. ACS Energy Letters, 2020, 5(8): 2698-2705.

5 Yang B, Zhang Z, Liu P, et al. Flatband λ-Ti3O5 towards extraordinary solar steam generation[J]. Nature, 2023, 622(7983): 499-506.

6 Wang Y, Zhu W, Du W, et al. Cocrystals Strategy towards Materials for Near-Infrared Photothermal Conversion and Imaging[J]. Angewandte Chemie, 2018, 130(15): 4027-4031.

7 Chen G, Sun J, Peng Q, et al. Biradical-featured stable organic-small-molecule Photothermal materials for highly efficient solar-driven water evaporation[J]. Advanced Materials, 2020, 32(29): 1908537.